Imaging magnetic flux-closure domains and domain walls in electroless-deposited CoNiB nanotubes – Supplementary

M. Staňo,[1,*] S. Schaefer,[2] A. Wartelle,[1] M. Rioult,[3] R. Belkhou,[3] A. Sala,[4] T. O. Menteş,[4] A. Locatelli,[4] L. Cagnon,[1] B. Trapp,[1] S. Bochmann,[5] S. Martin,[1,6] E. Gautier,[6] J. C. Toussaint,[1] W. Ensinger,[2] and O. Fruchart[1,6,†]

[1] *Univ. Grenoble Alpes, CNRS, Institut NEEL, F-38000 Grenoble, France*
[2] *Technische Universität Darmstadt, D-64287 Darmstadt, Germany*
[3] *Synchrotron SOLEIL, Saint-Aubin BP 48, F-91192 Gif-sur-Yvette, France*
[4] *Elettra - Sincrotrone Trieste S.C.p.A., I-34012 Basovizza, Trieste, Italy*
[5] *Friedrich-Alexander University of Erlangen-Nürnberg, D-91058 Erlangen, Germany*
[6] *Univ. Grenoble Alpes, CNRS, CEA, SPINTEC, F-38000 Grenoble, France*

(Dated: April 21, 2017)

CONTENTS

* michal.stano@neel.cnrs.fr
† olivier.fruchart@cea.fr

I. ELECTROLESS DEPOSITION

Electroless deposition is a very flexible and powerful tool for the conformal coating of metal thin films on arbitrary substrates [1, 2]. In comparison to other plating techniques such as electrodeposition, atomic layer deposition, chemical and physical vapour deposition techniques, no special equipment or requirements are needed. The deposition process is based on the autocatalytic reaction of the metal ions inside the plating solution at a specially functionalized surface. For the preparation of nanostructures, such as nanotubes, a template providing the proper shape is needed, such as an ion track-etched polymer foil.

A. Chemicals

All glassware was cleaned with nitric acid and aqua regia before use. The solutions were prepared freshly with Milli-Q water ($> 18\,\mathrm{M\Omega \cdot cm}$ at room temperature). The following chemicals were used without further purification: cobalt(II) sulphate heptahydrate (Sigma, 99.0%), dichloromethane (Promchem, 99.8%), borane dimethylamine complex – DMAB (Aldrich, pur 97%), ethanol (Labor Service GmbH, p.a.), potassium chloride (Merck, pur 99,5%), nickel(II) sulphate heptahydrate (Sigma, 99,0%), methanol (AppliChem, pure Ph. Eur.), palladium(II) chloride (Sigma, 99.9%), sodium citrate dihydrate (Sigma, puriss.), sodium hydroxide 32% in water (Sigma Aldrich, purum), tin(II) chloride (Merck, for synthesis), trifluoroacetic acid (Riedel-de Haën, $> 99\%$), and iron(II) sulphate heptahydrate (Sigma, 99%).

B. Template preparation

As a template, ion-track etched polycarbonate membranes are used. The track formation and track etching process is explained in literature [3]. For the synthesis of CoNiB and NiFeB nanotubes a 30 µm-thick polycarbonate (PC) foil (Pokalon from LOFO, High Tech Film GmbH) was irradiated with Au^{26+} ions (fluence: 10^7 ions/cm^2; kinetic energy of the projectile: 11.4 MeV per nucleon) at the GSI Helmholtzzentrum für Schwerionenforschung GmbH (Darmstadt). The latent ion tracks were etched out at 50 °C in 6M stirred sodium hydroxide solution for 11 min. The as-prepared template with cylindrical pores is washed with water and dried.

C. Radial growth in pores

After the functionalization of the template surface by sensitizing with a $SnCl_2$-solution [42 mM $SnCl_2$ and 71 mM trifluoroacetic acid in methanol and water (1:1)] and activating with $PdCl_2$-solution [11.3 mM $PdCl_2$, 33.9 mM KCl], the template is immersed in the deposition solution, which contains 100 mM $NiSO_4 \cdot 7H_2O$, 30 mM $CoSO_4 \cdot 7H_2O$, 100 mM sodium citrate dihydrate, and 100 mM dimethylamine borane. The deposition takes place at room temperature and starts at the pore walls on the catalytic Pd seed particles and continues radially towards the pore centre (Supplementary Fig. 1). During the synthesis, hydrogen gas evolves at the template surface as a part of the deposition reaction.

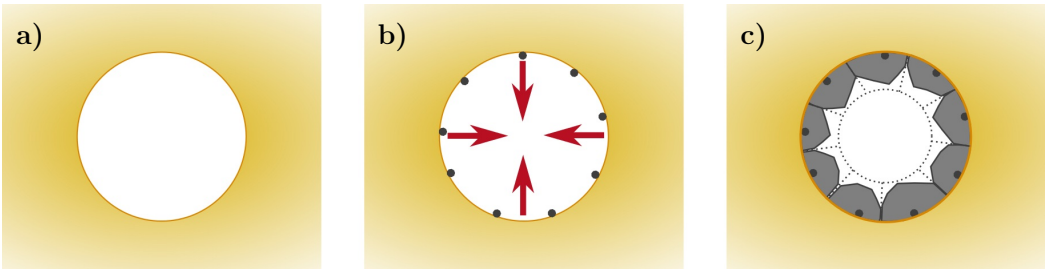

Supplementary Fig. 1. **Scheme of the radial metal growth.** Cross-section of a cylindrical pore in the polycarbonate foil. a) Empty pore. b) Functionalized polymer surface through Pd-seeds on the pore walls. The arrows show the growth direction of the desired metal (Co, Ni). c) Metal grows radially from the pore interface inwards. The final states is indicated by the dotted lines.

II. CHARACTERIZATION OF THE TUBES

A. Chemical analysis

We used two techniques for chemical analysis of our tubes, namely Energy Dispersive X-ray Spectroscopy and Electron Energy Loss Spectroscopy. The former was employed in scanning electron microscope to probe sample area in tens or hundreds of nanometres. The later was used in scanning transmission electron microscope for analysis on the scale of few nanometres.

Chemical analysis by Energy Dispersive X-ray Spectroscopy (EDX) was performed utilizing Zeiss ultra+ microscope with Bruker Quantax EDX. The analysis was conducted using different primary electron beam energies on both clusters and single tubes on a Si substrate as well as single tubes on a lacey carbon grid for transmission electron microscopy (TEM).

Primary beam energies of 15 and 20 keV were used for the precise determination of ratio of metals ($Co_{80}Ni_{20}$), whereas much lower energies ($\leq$ 5 keV, namely 3.0, 4.5, and 5.0 keV) and single tubes on the TEM grid were used in order to detect boron (B-K_α: 183 eV). Here boron comes from the reducing agent used during the deposition. It influences the microstructure of the deposit, with more boron leading to finer grains and eventually to amorphous material [4].

Such a light element as boron is very difficult to detect with EDX, for some systems even impossible. Several ingredients are needed for boron detection: low primary beam energy (otherwise the Boron signal is hidden in the background), silicon drift detector with a very light window transmitting B-K_α radiation [5]. Even with these the excitation of characteristic X-rays is low, window absorption high and detector efficiency low. In addition, part of the B-K_α can be absorbed by CoNi and carbon layer (contamination unavoidable, especially as the tubes come from the polycarbonate template). The best results were obtained on single tubes suspended above vacuum - no substrate contribution. An example of the EDX spectrum of a single tube acquired with 4.5 keV primary beam energy is shown in Supplementary Fig. 2. The presence of boron is clear (also for primary beam energy of 3.0 keV and 5.0 keV).

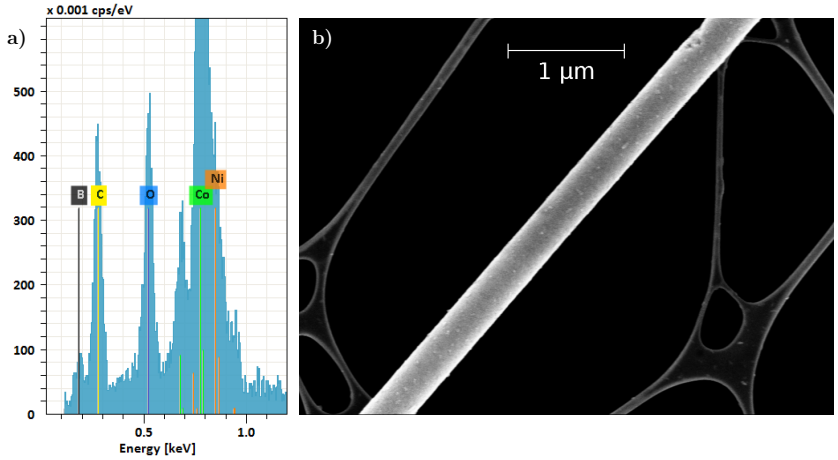

Supplementary Fig. 2. **Chemical analysis using EDX.** a) EDX spectra acquired with low primary beam energy (4.5 keV) showing the boron presence aside from expected Co and Ni, as well as C and O coming mainly from the template dissolution and possibly partial tube oxidation for the later element. b) Electron microscopy image of the investigated tube on a lacey carbon film. EDX spectrum taken in the middle of the tube. Similar results were obtained at different points as well as when averaging over larger tube area.

As for the quantification of the boron presence, we could not obtain reliable results with EDX due to very low counts on the detector. Depending on the primary beam energy and quantification method, the figure for boron content ranged from a few up to 30 % at. In the literature, X-ray Photoelectron Spectroscopy (XPS) on significantly larger tubes (same concentration of the reducing agent) suggested a negligible B content [6], while Richardson et al. [7] found with XPS around 25% at of boron in electroless-deposited tubes using the same reducing agent (DMAB). They measured similar content for different deposited metals and alloys, concentration of metallic salts in the bath. The Boron content increased with lower pH of the plating bath; it should be also influenced by the concentration of the boron containing reducing agent (DMAB). In our case, on one hand the concentration of boron species in solution was lower (decreases B in the deposit), on the other hand the pH of the bath is slightly lower (increases B in the deposit). Altogether we expect a similar or slightly lower amount of boron in our tubes than reported by Richardson

(25% at).

Aside from above-mentioned elements (Co, Ni, B), sometimes traces of Pd (seed particles in the deposition) and Sn (template modified with Sn(II) species) were detected with EDX as well. The presence of C and O is attributed mainly to the dissolution of the polymeric template, TEM grid with the C film, and unavoidable partial carbon contamination and surface oxidation.

Preliminary Electron Energy Loss Spectroscopy measurements suggest that the grains (clusters) are rather metallic with the boundaries being rich in oxygen. Experiments in the range of energies including boron (around 200 eV) will be done later. These should confirm whether boron is concentrated also in the grain boundaries as suggested by Geng et al. [8].

B. Transmission electron microscopy

Supplementary Fig. 3 shows a transmission electron microscopy image of a CoNiB tube. The material appears to be made of many small grains (around 10 nm or even smaller) and their boundaries appear bright. This could be explained by a smaller thickness or more likely lighter elements such as boron in-between the grains – such structure, metallic grains in a boron matrix, was already suggested for similar electroless-plated materials (Ni-B) [8]. The cross-section of the tube wall reveals a thickness approximately 30 nm, with both inner and outer surfaces covered with either remains of the dissolved polymeric matrix, and/or slightly oxidized.

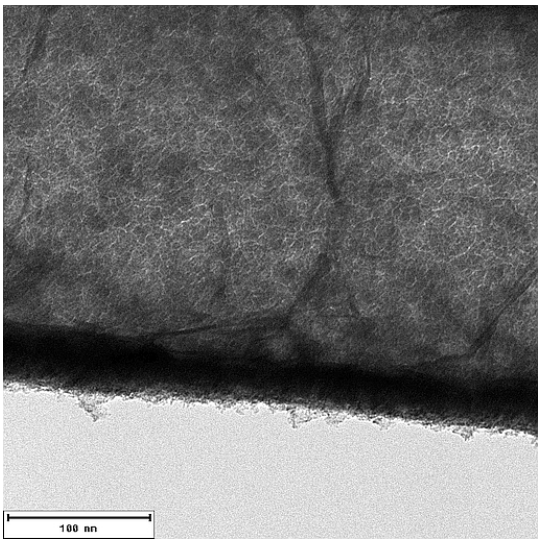

Supplementary Fig. 3. **Transmission electron microscopy image of a CoNiB tube.** The tube is composed of many small grains (around 10 nm or even smaller). Grains boundaries appear brighter which could be explained by smaller thickness or more likely amorphous boron in between the grains - such structure (metallic grains in boron matrix) has been already suggested for similar electroless-plated materials [8]. The tube wall thickness is approximately 30 nm. Both inner and outer tube surface is covered with rests of the dissolved polymeric matrix and possibly they are also slightly oxidized.

C. Magnetometry of single tubes and arrays

We performed hysteresis loops both on arrays of tubes still in a template (magnetometry with VSM-SQUID) and single (isolated) tubes (magneto-optics with focused laser).

Supplementary Fig. 4a shows a hysteresis loop obtained for an array of CoNiB tubes in a polycarbonate matrix with magnetic field applied along the tubes. The pore density is very low and the hollow nature of tubes reduces the total moment compared with wires of identical diameter (Supplementary Fig. 4b), so that we expect weak magnetostatic interactions, contrary to the case of anodized alumina templates and solid nanowires [9].

Single tubes dispersed on a Si substrate were probed by the Magneto-Optical Kerr Effect (MOKE), implemented in the longitudinal configuration with a focused He-Ne ($\lambda = 632.8$ nm) laser (spot 1 µm). The field was swept as a triangular wave signal, with frequency 1.1 Hz, and field calibration uncertainty max ±5 mT. In order to limit the

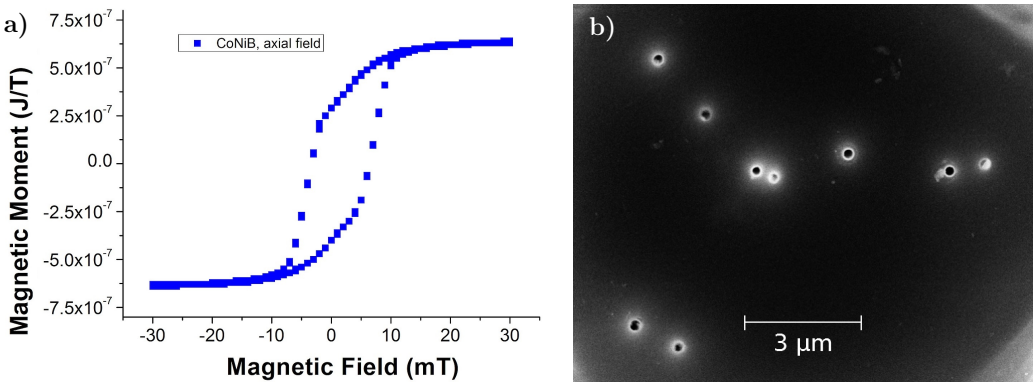

Supplementary Fig. 4. **Magnetometry on array of tubes.** a) Hysteresis loop on a sparse array (low density, low interactions) of CoNiB tubes in the polycarbonate template, measured by VSM-SQUID. The field is applied parallel to tube axis. b) Scanning electron microscopy, top view of a part of the measured template illustrating the low density of pores.

potential effect of heating, the laser power was set to 0.2 mW. Commonly even few mW laser power is used for investigation of magnetic nanostructures. Supplementary Fig. 5 shows a typical loop obtained under such conditions.

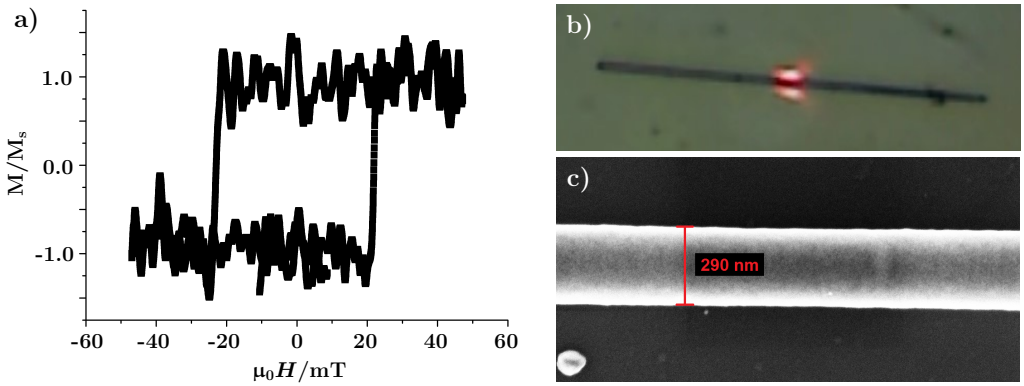

Supplementary Fig. 5. **Magnetometry on a single tube - magnetooptics with focused laser.** a) Hysteresis loop for the axial magnetic field. Average of 100 loops with short acquisition time (0.9 s, 5000 points each loop), LeCroy noise filter 2.5 bits applied [10]. b) Optical image (magnification 100x) with the laser spot, the magnetic field is applied in the horizontal direction, close to parallel to the tube axis. c) Scanning electron microscopy image of a central part of the investigated tube.

Thus, both global and single-tube measurements agree on switching or saturation fields in the range (10-25 mT). Note that some loops measured with MOKE were also slanted similar to the global magnetometry but still with a higher squareness. This is consistent with the values of saturation field evidenced with STXM(section IV B).

III. THEORY AND SIMULATIONS

A. Phase diagram for the magnetization state in tubes

Escrig [11], Landeros [12], and Sun [13] and coworkers presented phase diagrams for magnetically soft nanotubes (considering exchange and magnetostatic energy) as a function of tube diameter, tube wall thickness and length. They predicted areas with either axial magnetization (possibly with localized curling close to the tube ends), or curling along the entire tube (orthoradial magnetization). The uniform orthoradial state is the ground state only for short tubes with a large diameter (small aspect ratio) and large tube wall thickness, all to be compared with the dipolar exchange length. In addition, the models in [11, 13] overestimate the magnetostatic energy for longitudinal magnetization state, which can be reduced by creation of end curling features [12–14]. In other words, tubes with axial magnetization are expected to occupy an even larger part of the phase diagram, as shown in [12]. Recently, these two distinct behaviours depending on the tube geometry were confirmed experimentally by Wyss and coworkers [15].

Based on this, tubes with our geometry should undoubtedly display axial magnetization, were they made of a magnetically-soft material. This is a proof that another energy term, favouring orthoradial magnetization, exists in our material.

B. Bloch and Néel walls in magnetic nanotubes

In thin films, the domain wall (DW) type, Bloch vs Néel, depends mainly on the film thickness. The transition is reported around 20-40 nm for 180° DWs and magnetically-soft films. However, it can be affected by an additional magnetic anisotropy, such as magnetocrystalline [16]. We found a similar trend in the micromagnetic simulations of our nanotubes with orthoradial domains, where Néel-like DWs are favoured for small tube wall thickness and Bloch-type DWs for larger ones. As in the simulations we promote the orthoradial domains by defining the tube axis as a hard axis (uniaxial effective anisotropy), Bloch walls are preferred for larger anisotropy constants. A more systematic study of geometries with a different way of promoting the orthoradial magnetization (*orthoradial easy axis*) can be done to build a phase diagram of the DWs.

Aside from modelling of small tubes (diameter 50 nm) we performed micromagnetic simulations [17] for tubes with diameter 120 nm, tube wall thickness 30 nm and length of 1000 nm. The end charges are compensated in the calculation of the dipolar field, to mimick an infinitely-long structure. The simulation parameters follow: spontaneous induction $\mu_0 M_s = 1.0\,\mathrm{T}$, exchange stiffness $A = 10\,\mathrm{pJ/m}$, cell (tetrahedron) size max 4 nm, and effective uniaxial anisotropy with hard axis along the tube and anisotropy constants $30\,\mathrm{kJ/m^3}$ and $100\,\mathrm{kJ/m^3}$ for Néel and Bloch walls, respectively. The simulation provides results similar to the ones for smaller tubes, only the extent of Bloch-like DWs with respect to the tube diameter is smaller. This results in a very small tilt of the domain boundary in consequent XMCD-PEEM contrast modelling, which is why we illustrated the main text with smaller diameters, for clarity.

For a better visualization of the micromagnetic configuration of Bloch and Néel DWs, we display the tube outer surface as if unrolled (Supplementary Fig. 6). Note that maps are very similar for the inner surface. The maps show the three cylindrical components of magnetization: M_z (axial direction), M_ϕ (orthoradial/azimuthal direction), and M_r (radial direction). Unlike for smaller diameters, the Bloch wall is associated with a weak (but non-negligible) bipolar axial component of magnetization, and the Néel wall with a weak bipolar radial component. These, which do not occur for flat thin films, result from the rolled geometry and the bipolar line of charge, which breaks the symmetry between the inner versus outer surface.

C. More on Bloch like walls

In the main text we mentioned that in XMCD-PEEM images with the beam perpendicular to the tube axis we observe a tilted domain boundary on the tube surface for Bloch-like DWs (Fig. 4a,b in the main text). In the experiments, in the majority of cases in a given tube, the tilt is the same for all DWs. As the domains alternate, this means that the DW contrast at the tube front and back alternates between successive DWs. Therefore the radial magnetization points alternatively inwards and outwards (alternating domain wall *polarity*). This case is shown in Supplementary Fig. 7a, while Supplementary Fig. 7b shows the case with DWs having the same radial component. The former allows a better closure of the flux and as a result is found to be of lower energy, which may explain its predominance in the experiments.

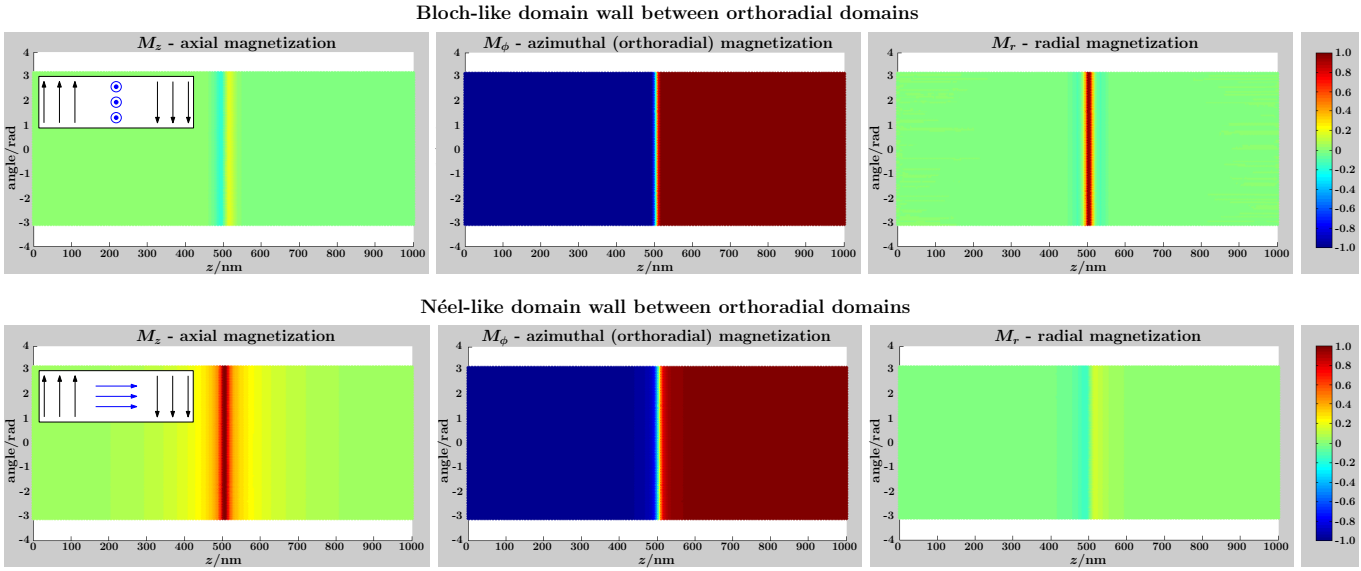

Supplementary Fig. 6. **Unrolled maps of magnetization for Bloch (top) and Néel (bottom) DWs in between two orthoradial flux-closure domains.** The maps feature the three components of magnetization of the outer surface for a tube with diameter of 120 nm and tube wall thickness of 30 nm. The effective anisotropy constants (hard axis along the tube) are 30 kJ/m^3 and 100 kJ/m^3 for Néel and Bloch walls, respectively. The domain walls are located in the middle of the maps, in between 2 orthoradial flux-closure domains with opposite curling sense, which can be seen on the M_ϕ map - opposite sign on either side of the wall. Insets in M_z panels show corresponding idealized Bloch and Néel walls in thin films / unrolled tubes.

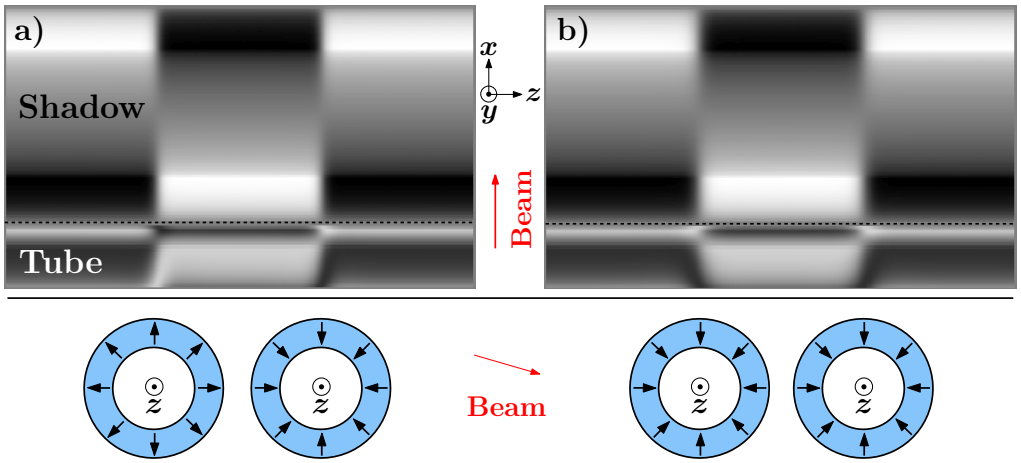

Supplementary Fig. 7. **Simulated XMCD-PEEM contrast for two Bloch DWs separating three orthoradial domains with alternating circulation.** DWs with (a) opposite and (b) same radial components (*polarity*). Simulations are based on small tubes (diameter 50 nm, tube wall thickness 10 nm) and only partially relaxed micromagnetic configurations (not necessarily stable for this geometry). Still it reflects well the main qualitative differences between the two configurations.

IV. ORTHORADIAL MAGNETIC ANISOTROPY

A. Modelling of orthoradial magnetic anisotropy

Here we provide arguments for describing and extracting the strength of the microscopic magnetic anisotropy favoring orthoradial magnetization. First, the question arises of the functional form relevant to describe the volume density of magnetic anisotropy, as none of the three local directions are equivalent: radial $\hat{\mathbf{r}}$, orthoradial $\hat{\boldsymbol{\phi}}$ and axial $\hat{\mathbf{z}}$. As the magnetic field needed to align magnetization along the tube axis (around 25 mT, Supplementary Fig. 4a, 5, and 8f) is two orders of magnitude smaller than magnetization (spontaneous induction 1 T), we assume that local shape anisotropy is the dominant energy term. Therefore we suppose that radial magnetization $m_r = 0$ in domains. Thus, describing the anisotropy with terms $-K_\phi m_\phi^2$ or $K_\phi m_z^2$, because $m_\phi^2 + m_z^2 \approx 1$. $K_\phi > 0$ favours orthoradial magnetization.

On the basis of the moderate wall thickness, we assume that radius-dependent variations are averaged out and taken into account in an effective uniform value of K_ϕ. A first contribution to K_ϕ is anisotropy related to the lattice K_{mc} (magnetocrystalline, magnetoelastic or interface, to be discussed in the next section). A second contribution is related to exchange energy, whose volume density reads, for $m_r = 0$ [13, 18]: $E_{\mathrm{ex}} = (A/R^2)m_\phi^2$ with A being the exchange stiffness constant and R the tube radius. The reason for this term is that curvature induces a spatial variation of magnetization for a uniform m_ϕ, due to the non-uniformity of $\hat{\boldsymbol{\phi}}$. Uniform m_z is associated with no spatial variation, so that it does not contribute. The total anisotropy coefficient is therefore $K_\phi = K_{\mathrm{mc}} - A/R^2$. This can be converted into an anisotropy field $H_K = 2K_\phi/(\mu_0 M_{\mathrm{s}})$. Measuring the latter experimentally allows one to estimate the microscopic anisotropy energy coefficient: $K_{\mathrm{mc}} = A/R^2 + \mu_0 M_{\mathrm{s}} H_K/2$.

B. Experimental determination of the anisotropy strength

Experimentally, we estimated H_K based on a series of Scanning Transmission X-ray Microscopy (STXM) images acquired under different external magnetic field applied along the tube axis (Supplementary Fig. 8). Upon increasing the field, the domain contrast decreases, which shows that magnetization gradually rotates towards the axial direction. It is difficult to extract quantitatively the direction of magnetization in this series, because of the exponential decay of photon intensity inside matter, uncertainties in the dichroic coefficient, and the existence of a background intensity in the image. We can only provide an estimate of the H_K from the fields where all contrast vanishes in the corresponding images. We find $\mu_0 H_K \approx 25$ mT. This value is consistent with global and single-tube magnetometry mentioned above in section II C. Note that at remanence the tubes return to a flux-closure domain pattern, and that the series with the opposite direction of applied field is very similar.

As regards the conversion of H_K to the anisotropy constant, we do not have a direct measurement of the exchange stiffness of our material, however for example $Co_{80}B_{20}$ has around $A = 10$ pJ/m [19]. This value may be different in our case, but the order of magnitude should be correct. Besides, the tube diameter is large, so that the exchange penalty correction to the anisotropy is rather small, less than few mT of equivalent field, which might be well within the error/spread of the experimentally determined anisotropy field. Therefore we arrive at an estimate of the anisotropy constant $K_{\mathrm{mc}} \approx 10\,\mathrm{kJ/m^3}$. However, this value may be affected by a sample ageing. The one-year-old sample, initially used for XMCD-PEEM and later for STXM, shows less sharp orthoradial domains and a weak axial component of the magnetization, although it has been kept under primary vacuum. Therefore, the initial value (giving well defined orthoradial domains with Bloch like domain walls) may have been higher.

C. Possible microscopic sources of orthoradial anisotropy

As our tubes are cobalt-rich, the first contribution coming to mind is the magnetocrystalline anisotropy. However, as our tubes are nanocrystalline with a random texture (see Fig. 1 in the main text), we rule out the magnetocrystalline contribution. There must be another source of magnetic energy, for which the degeneracy between the axial $\hat{\mathbf{z}}$ and the orthoradial $\hat{\boldsymbol{\phi}}$ direction is lifted. While both directions are normal to the radial direction $\hat{\mathbf{r}}$, and are thus locally similar to two the in-plane direction for a thin film, the difference is the existence of curvature along the orthoradial direction. We consider below two possible sources of magnetic anisotropy that could arise from the direction-dependent curvature: intergranular interface anisotropy and magnetoelasticity. As mentioned in the main text, owing to the radial growth process, grains are expected to have their shape and size varying differently along the two directions. We detail below handwaving models, and show that both sources could in some cases provide a strength of anisotropy whose order of magnitude is consistent with the experimental data.

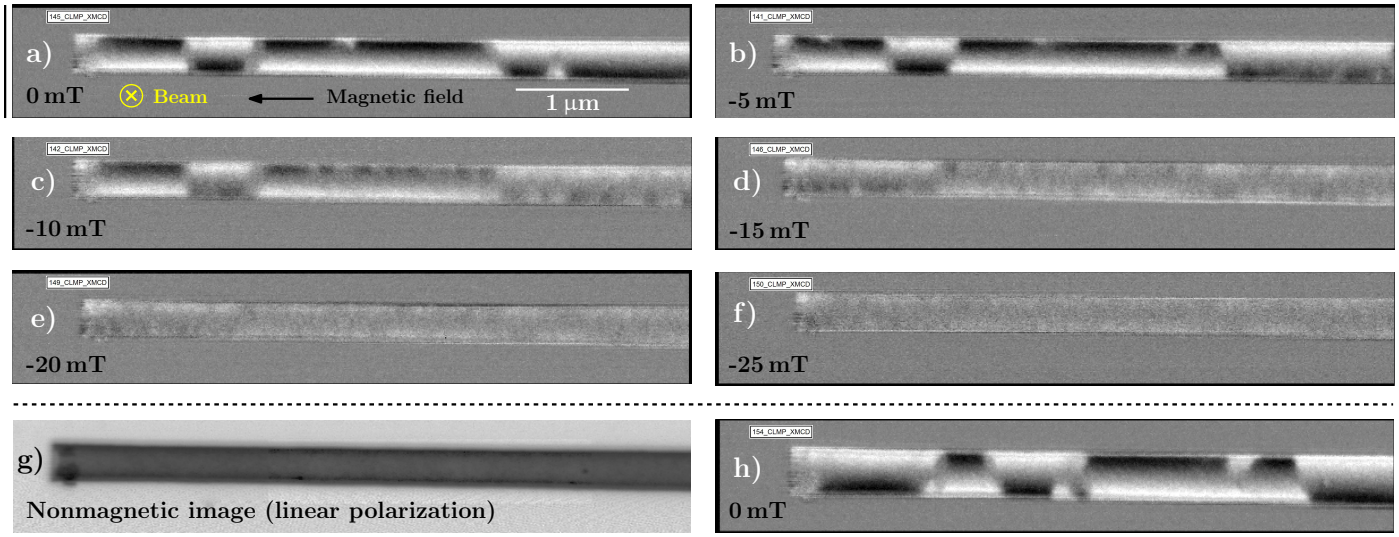

Supplementary Fig. 8. **STXM under external magnetic field - anisotropy strength determination**. a)-f) XMCD magnetic images (same contrast range 15%) under axial magnetic field. With increasing the field magnitude the STXM contrast vanishes, showing that magnetization rotates towards the axial direction. Around 25 mT is needed for the saturation of tubes along the axial direction. Field of view a)-g) $6.0 \times 1.0\,\mu m^2$ and h) $6.0 \times 0.8\,\mu m^2$. g) Nonmagnetic STXM image (linear polarization of X-rays) highlighting the tubular structure. h) XMCD image after removing magnetic field (after sequence a-f, image size $6.0 \times 0.8\,\mu m^2$). Even at zero field, the transition between neighbouring domains is not as sharp as in XMCD-PEEM images; this we attribute to sample ageing (STXM done 1 year after X-PEEM, samples kept under primary vacuum).

First we discuss the interface anisotropy. As our samples are nanocrystalline, the ratio of atoms in the vicinity of a grain/cluster boundary is not negligible, so that interface anisotropy K_s with e.g. boron-rich grain boundaries could arise. We consider a tube with outer diameter 250 nm and wall thickness 25 nm. Assuming an isotropic grain size upon nucleation from the outer diameter, the orthoradial grain size at the inner diameter should be reduced by 20 %, so that on the average along the radius the anisotropy of grain size $\delta = \frac{\langle l_z \rangle - \langle l_\phi \rangle}{(\langle l_z \rangle + \langle l_\phi \rangle)}/2$ is 0.1, yielding a slightly wedge-shaped grain (such as in Supplementary Fig. 1c). Transmission electron microscopy suggests that the grain size is of the order of $t = 10$ nm . The anisotropic contribution K_{eff} of K_s to the effective volume magnetic anisotropy is therefore $2\delta K_s/t$. Considering $K_s \approx 0.2\,mJ/m^2$ as an estimate (values one order of magnitude higher may exist at some interfaces, for instance between 3d elements and some oxides [20]), one finds: $K_{eff} \approx 4 \times 10^3\,J/m^3$. Expressed in anisotropy field: $H_{eff} \approx 2K_{eff}/(\mu_0 M_s) = 8 \times 10^3\,A/m$, or: $\mu_0 H_{eff} \approx 10\,mT$. This is of the same order of magnitude as the measured value of 25 mT. Another contribution of interface anisotropy may be due to the curvature of the outer and inner parts of the grains, so that the orientation of atomic bounds is on the average slightly different along the axial and orthoradial directions. A modelling would however require advanced information about the structure of the interface, which is not available.

We now discuss the magnetoelastic anisotropy. Borides of 3d ferromagnetic elements are known to display sizeable magnetoelastic effects[21] (except for $(Ni_{80}Fe_{20})B$ with almost zero magnetostriction; NiFeB tubes are described below), and electroless plating is also known to deliver strained materials. It is probable that the expected wedged shape of the grains described above (also see Supplementary Fig. 1c), induce a building of compressive strain ϵ along $\hat{\boldsymbol{\phi}}$ while the grain grows inward, because there is less and less space to accommodate incoming atoms. Note that no source of strain is expected along $\hat{\mathbf{z}}$, as the dimension of the grain stays the same as there is no curvature along the axis. Nevertheless, tensile strain may be expected from elastic theory, as a reaction to the compressive along $\hat{\boldsymbol{\phi}}$. An extra isotropic strain in the $(\hat{\boldsymbol{\phi}}, \hat{\mathbf{z}})$ plane may also be expected from the electroless deposition. The saturation magnetostriction of Co-rich CoNi borides is of the order of $\lambda \approx -6 \cdot 10^{-6}$, more values with references can be found in Tab. I. For 3d metals the combination of elastic coefficients $c_{11} - c_{12}$ is of the order of $10^{-11}\,N/m^2$, or $10^{-11}\,J/m^3$. Thus, the linear magnetoelastic coefficient is $B_1 \approx -10^6\,J/m^3$. An anisotropy of strain of 0.4 % would therefore be required to account for the observed microscopic anisotropy.

To conclude this part, electroless-grown materials are expected to develop nanograins with some anisotropic structure features along the orthoradial and axial directions, associated with the local curvature of the supporting surface, be it shape or strain. A resulting contribution to magnetic anisotropy is expected, which could arise from both interface anisotropy and magnetoelastic coupling. Realistic figures show that both sources are consistent to explain experimental results. Without further knowledge on the structural anisotropy of the nanograins, which would be

challenging to access, it is not possible to decide which phenomenon is dominating.

Supplementary Tab. I. **Saturation magnetostriction λ_s for some Co-rich CoNiB compounds.**

material	λ_s	reference
$(Co_{80}Ni_{20})_{80}B_{20}$	$-5 \cdot 10^{-6}$	[21]
$Co_{80-x}Ni_xB_{20}$	$-7 \cdot 10^{-6}$ for $x \in (0; 12)$	[22]
$(Co_{80}Ni_{20})_{77}B_{23}$	$-8 \cdot 10^{-6}$	[23]

V. NiFeB TUBES WITH AXIAL MAGNETIZATION

As mentioned in the main text, $(Ni_{80}Fe_{20})B$ tubes (diameter 350-390 nm) were fabricated using the same electroless deposition technique and templates, only cobalt (II) sulfate in the plating solution was replaced by iron (II) sulfate. These tubes are grown also in confined pores and the growth proceeds radially, therefore similar strain could be expected. However, unlike CoNiB, these NiFeB tubes have almost zero magnetostriction [21] and therefore the magnetoelasticity is negligible. In addition, Fe-based alloys are also known to display lower interfacial anisotropy. In other words, both above-discussed anisotropy sources are expected to be weaker in magnitude. Consistently, we found out that tubes of this material are axially magnetized (Supplementary Fig. 9).

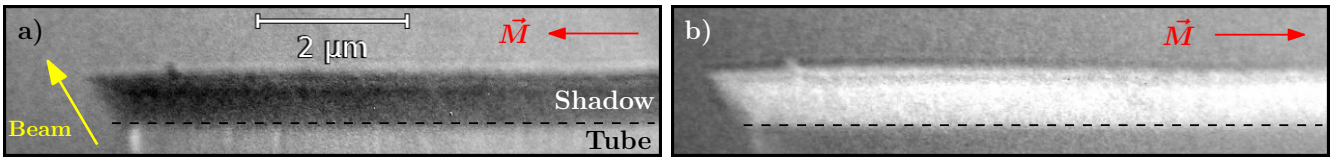

Supplementary Fig. 9. XMCD-PEEM images of an electroless-deposited NiFeB shell magnetized axially sequentially along two opposite directions. The beam arrives from the bottom in a direction depicted by the arrow. Only the shadow area (information from the volume) is clearly visible due to selected focus on the shadow and partial oxidation of the outer tube surface. The tube is axially magnetized with magnetization component a) parallel and b) anti-parallel to the X-ray beam. The magnetization was switched by applying 15 mT along the tube axis. Switching field of these tubes is 10-15 mT.

VI. ANNEALING OF CoNiB TUBES

A. Defects upon annealing

Upon annealing under vacuum in the PEEM chamber, hollow defects appeared in the shell of some CoNiB tubes, for temperatures typically above 450 °C. These holes are visible both in X-PEEM and subsequent scanning electron microscopy images (Supplementary Fig. 10a, here an extreme case being shown). Not all tubes had the same density of holes upon the same annealing (Supplementary Fig. 10b), which may come from variation in tube wall thickness. Some tubes do not display any visible damage.

As the calibration of temperature for the in-situ PEEM-chamber annealing is not accurate, for comparison we performed annealing experiments in a separate vacuum furnace with a better control of temperature as both the substrate and the environment are at the same temperature. Now we will briefly mention possible differences in experimental conditions between annealing done inside the PEEM chamber (in-situ annealing) and the vacuum furnace annealing but we do not suppose that they play a significant role. The PEEM chamber is operated under ultra-high vacuum. However, during annealing the pressure increases substantially and it is of the same order of magnitude as the pressure in the vacuum furnace (secondary vacuum, $< 10^{-4}$ Pa). The main difference might be X-ray beam irradiation of some tubes before the annealing, in particular effect of the X-rays on the tubes and impurities that cover them (breaking bonds, graphitizing hydrocarbons, etc.). As only part of the sample was irradiated, but the whole sample was annealed, we could conclude that there is no big difference between irradiated tubes and tubes not exposed to X-rays (based on electron microscopy images of both sets of tubes). As we used twin samples on the same substrates in both (in-situ, furnace) annealing experiments, we suppose that both are comparable.

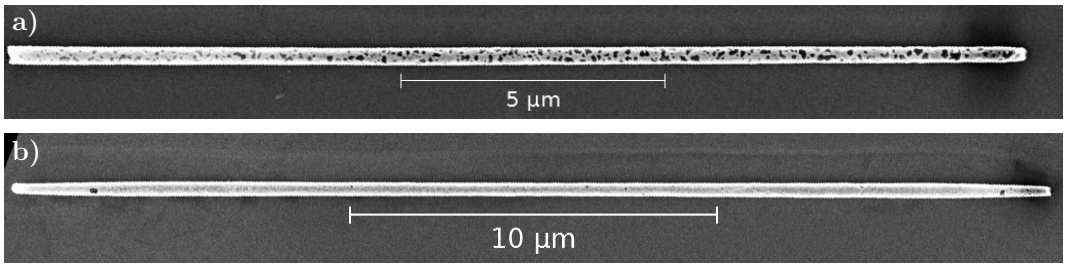

Supplementary Fig. 10. **Defects upon in-situ annealing** (500 °C ± 50 °C). SEM images of two tubes lying on the same substrate, displaying very different amount of defects after annealing. Both tubes displayed axial magnetization after annealing. The difference may come from a variation in the tube wall thickness.

Even the furnace annealing (at least 30 min, secondary vacuum) provided tubes both with and without significant defects for temperatures 450 °C, 500 °C, 550 °C, and 600 °C. Still more defects in larger amount of tubes appear with increasing temperature, especially above 550 °C. For a lower temperature, 400 °C, no significant defects were present, but on the other hand the transformation to axial magnetization was not complete. At 550 °C most of the tubes are severely damaged with many holes, only a minority of tubes is rather intact and some tubes survive also up to 600 °C. Therefore optimal annealing temperature seems to be 450 °C − 500 °C. Further, we have tried shorter (15 min) and longer (150 min) annealing time for 450 °C. 15 min led to almost no defects, but the increase of the grains size with respect to the as-deposited sample was very small, suggesting that longer annealing is needed. Longer (150 min) experiment produced slightly more defects such as tubes broken in places where there were already some small defects. The presence of larger defects (especially above 400 °C) can be an issue as they lead to inhomogeneity in the magnetic configuration. We tried to tackle this problem fortifying the tubes with an additional inner (non-magnetic) layer deposited either by electroless plating or atomic layer deposition (ALD). It seems that the amount of defects in such tubes upon annealing is lower. Alternatively it is possible to perform the ALD after dispersion of tubes on the substrate - this improves not only mechanical stability, but also protects the tubes from further oxidation. But we refrained from such treatment as the electrically-insulating oxide cover layer can cause problems (charging) in collecting photoelectrons in XMCD-PEEM.

B. Decrease of the XCMD-PEEM contrast upon annealing (Fig. 5 in the main text)

In the main text, in particular in Fig. 5, we attributed the loss of the XMCD-PEEM contrast upon annealing to a gradual rotation of magnetization towards the axial direction. Other possible explanations could include transverse magnetization close-to-perpendicular to the beam direction and/or decrease of magnetic moment. Both cases are highly improbable, as an external magnetic field would be required to sustain the transverse magnetization and similar electroless-deposited materials are known to increase their magnetic moment upon annealing [7].

C. XMCD-PEEM: reversal of in-situ annealed tubes

After the in-situ annealing, magnetization of the CoNiB tubes is longitudinal. We used a coil fitted in the XMCD-PEEM sample cartridge to apply magnetic field to these tubes. A few mT applied along the tube axis were sufficient to fully reverse the magnetization direction (Supplementary Fig. 11). The contrast on the tube as well as in the shadow is weak, due to the close-to-perpendicular beam orientation with respect to the tube axes and thus the magnetization direction.

[1] Mallory, G. & Hajdu, J. *Electroless Plating: Fundamentals and Applications* (William Andrew Publishing/Noyes, 1990). American Electroplaters and Surface Finishers Society.

[2] Shacham-Diamand, Y., Osaka, T., Okinaka, Y., Sugiyama, A. & Dubin, V. 30 years of electroless plating for semiconductor and polymer micro-systems. *Microelectron. Eng.* **132**, 35–45 (2015). URL http://www.sciencedirect.com/science/article/pii/S0167931714003694. Micro and Nanofabrication Breakthroughs for Electronics, MEMS and Life Sciences.

[3] Apel, P. Y. & Dmitriev, S. Micro-and nanoporous materials produced using accelerated heavy ion beams. *Adv. Nat. Sci.: Nanosci. Nanotechnol.* **2**, 013002 (2011).

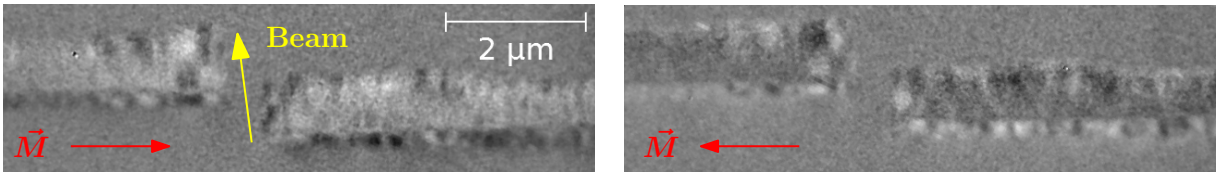

Supplementary Fig. 11. **Magnetic switching of annealed tubes with axial magnetization**. The magnetization in the axially-magnetized tubes can be reversed by applying a few mT along the tube axis, as seen from the left to the right image. There is a moderate distribution of switching field from tube to tube, however for a given one the same switching field is measured upon repeating the experiment. The beam arrives from the bottom of the image, and is close to perpendicular to the tube axes, so that the magnetic contrast is rather weak. Still one can distinguish the switch, both on the tube and in the shadow. In both images the left tube displays some orthoradial curling close to its end, as seen in the shadow. Both tubes display several defects (holes) due to over-annealing.

[4] Watanabe, T. *Nano plating* (Elsevier, 2004).

[5] Berlin, J. Analysis of boron with energy dispersive X-ray spectrometry. *Imaging & Microscopy* **13**, 19–21 (2011). URL https://www.bruker.com/fileadmin/user_upload/8-PDF-Docs/X-rayDiffraction_ElementalAnalysis/Microanalysis_EBSD/Articles/Repr_I_M_boron.pdf.

[6] Schaefer, S. *et al.* NiCo nanotubes plated on Pd seeds as a designed magnetically recollectable catalyst with high noble metal utilisation. *RSC Adv.* **6**, 70033–70039 (2016).

[7] Richardson, D. & Rhen, F. M. F. Increasing the magnetization of electrolessly deposited Ni–B nanotubes. *IEEE Trans. Magn.* **51**, 1–4 (2015).

[8] Geng, J., Jefferson, D. A. & Johnson, B. F. Exploring the structural complexities of metal–metalloid nanoparticles: The case of Ni · B as catalyst. *Chem. Eur. J.* **15**, 1134–1143 (2009).

[9] Velázquez-Galván, Y. *et al.* Dipolar interaction in arrays of magnetic nanotubes. *J. Phys. Condens. Matter* **26**, 026001 (2014). URL http://stacks.iop.org/0953-8984/26/i=2/a=026001.

[10] LeCroy. Application note 006 - Enhanced resolution in LeCroy digital oscilloscopes (1999). URL http://teledynelecroy.com/doc/digital-oscilloscopes-enhanced-resolution.

[11] Escrig, J., Landeros, P., Altbir, D., Vogel, E. & Vargas, P. Phase diagrams of magnetic nanotubes. *J. Magn. Magn. Mater.* **308**, 233–237 (2007).

[12] Landeros, P., Suarez, O. J., Cuchillo, A. & Vargas, P. Equilibrium states and vortex domain wall nucleation in ferromagnetic nanotubes. *Phys. Rev. B* **79**, 024404 (2009). URL http://link.aps.org/doi/10.1103/PhysRevB.79.024404.

[13] Sun, C. & Pokrovsky, V. L. Magnetic properties of a long, thin-walled ferromagnetic nanotube. *J. Magn. Magn. Mater.* **355**, 121 – 130 (2014). URL http://www.sciencedirect.com/science/article/pii/S0304885313009049.

[14] Chen, A., Usov, N., Blanco, J. & Gonzalez, J. Equilibrium magnetization states in magnetic nanotubes and their evolution in external magnetic field. *J. Magn. Magn. Mater.* **316**, e317–e319 (2007). URL http://www.sciencedirect.com/science/article/pii/S0304885307002466. Proceedings of the Joint European Magnetic Symposia.

[15] Wyss, M. *et al.* Imaging magnetic vortex configurations in ferromagnetic nanotubes. *arXiv:1701.01685* (2017). URL https://arxiv.org/abs/1701.01685.

[16] Xu, F. *et al.* Enhanced film thickness for Néel wall in soft magnetic film by introducing strong magnetocrystalline anisotropy. *Sci. Rep.* **6** (2016).

[17] http://feellgood.neel.cnrs.fr.

[18] Saxena, A., Dandoloff, R. & Lookman, T. Deformable curved magnetic surfaces. *Physica A* **261**, 13–25 (1998).

[19] Konč, M. *et al.* Temperature dependence of the magnetization and of the other physical properties of rapidly quenched amorphous CoB alloys. *IEEE Trans. Magn.* **30**, 524–526 (1994).

[20] Dieny, B. & Chshiev, M. Perpendicular magnetic anisotropy at transition metal/oxide interfaces. *Rev. Mod. Phys.* (2017). URL https://journals.aps.org/rmp/accepted/d8074Ea6X321130710ca4805f53402f69bc508a38. Accepted 28 November 2016.

[21] O'Handley, R. C. *Modern magnetic materials* (Wiley, 2000).

[22] Vlasák, G., Jergel, M. & Duhaj, P. Compositional dependence of magnetostriction of amorphous Co-Fe-B and Co-Ni-B alloys. *Mater. Sci. Eng.* **99**, 109–112 (1988).

[23] Yamasaki, J., Fukunaga, H. & Narita, K. Anisotropic magnetoresistance in transition metal-boron amorphous alloys. *J. Appl. Phys.* **52**, 2202–2204 (1981).